

# AIR-COUPLED ULTRASONIC BEAM TRANSMISSION APPLIED TO MATERIAL CHARACTERIZATION

Han Zhang<sup>†</sup> and D. E. Chimenti  
Center for NDE and  
Aerospace Engineering &  
Engineering Mechanics Department  
Iowa State University  
Ames IA 50011  
<sup>†</sup> Current address: Herzog Services, Inc, St Joseph, MO.

## INTRODUCTION

Lamb waves have been widely used in ultrasonic NDE to characterize material properties or assess material quality [1]. Of the previous work on materials using phase-matched fluid-loaded coupling, most has been performed in water-coupled testing [2]. With the development of efficient non-contacting ultrasonic air-coupled transducers [3], it has become feasible to apply air-coupled ultrasonic methods to NDE. Because of the low signal noise ratio resulting from the large impedance mismatch between the air and the solid object, most work of air-coupled (AC) ultrasound is qualitative, with defects in plates and C-scan imaging being the principal objectives. As demonstrated by Safaeinili, *et al.* [4], however, it is possible to characterize elastic plates, both isotropic and anisotropic, by using AC ultrasound, despite the signal-to-noise ratio (SNR) penalty.

Because of the inherent narrowband nature of the AC transducer, the traditional method of measuring the reflection coefficient as a function of frequency in immersion testing can not be extended to AC ultrasound; instead, a method developed by Safaeinili *et al* [4] to reconstruct the transmission coefficient as a function of angle at discrete frequencies is employed in this paper. We develop here an extended model and demonstrate how it can be used with an efficient inversion scheme to reconstruct transmission coefficients within the framework of a 2-D and 3-D transmitter voltage calculation based on the CTP. The difference between results obtained from the 2-D and 3-D voltage calculations will be shown.

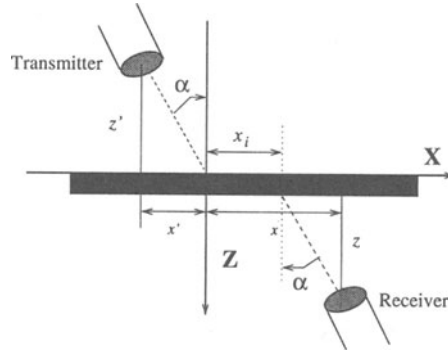


Figure 1. Schematic diagram of experimental transmission setup.

## THEORETICAL SUMMARY

We begin the transmission coefficient reconstruction with a spectral integral representation of the receiver voltage [5] in the geometry shown in Fig. 1,

$$V_{\mathcal{T}}(\alpha, x) = \frac{-1}{8\pi^2} \gamma(\omega) \omega \rho_f A_{\mathcal{T}} A_{\mathcal{R}} \int_{-\infty}^{\infty} \int_{-\infty}^{\infty} T(k_x, k_y) \times [\exp\{ik_x(\tilde{x} - \tilde{x}') + ik_y(\tilde{y} - \tilde{y}') + i\kappa_a(\tilde{z} - \tilde{z}')\}] / \kappa_a dk_x dk_y \quad (1)$$

where  $A_{\mathcal{T}}$  and  $A_{\mathcal{R}}$  specify the strength of the transmitter and receiver respectively,  $\gamma(\omega)$  is a temporal spectrum of the transducer electronics,  $\rho_a$  is the density of the air,  $\alpha$  is the transmitter and receiver angle, and  $b$  is the Fresnel length, given by  $b = k_a w_0^2 / 2$ , with the air wavenumber  $k_a = \omega / c_a$ ,  $c_a$  is the velocity in air, and  $w_0$  is the beam width at its waist.  $\kappa_a = \sqrt{k_a^2 - k_x^2 - k_y^2}$  is the wavevector projection on  $z$  axis. To convert the measured data to the wavenumber domain we construct a spatial Fourier transform,

$$S(\theta, \alpha) = \frac{1}{2\pi} \int_{-\infty}^{\infty} V_{\mathcal{R}}(x, \alpha) \exp(-ik_a \sin \theta x) dx. \quad (2)$$

The transformed 2-D signal of the calculated voltage is different from that of a 3-D calculated voltage, so we will treat them separately.

For the 2-D case there is no dependence on  $y$ , so we let  $k = k_x$  and  $\kappa_a = \sqrt{k_a^2 - k^2}$ . The voltage calculation formula Eq (1) becomes

$$V_{\mathcal{R}}(\alpha, x) = \frac{-1}{8\pi^2} \gamma(\omega) \omega \rho_f A_{\mathcal{T}} A_{\mathcal{R}} \int_{-\infty}^{\infty} T(k) \frac{\exp\{ik(\tilde{x} - \tilde{x}') + i\kappa_a(\tilde{z} - \tilde{z}')\}}{\kappa_a} dk. \quad (3)$$

The transformed signal corresponding to Eq (2) is

$$S(\theta, \alpha) = \frac{-1}{16\pi^3} \gamma(\omega) \omega \rho_f A_{\mathcal{T}} A_{\mathcal{R}} \int_{-\infty}^{\infty} \exp(-ik_a \sin(\theta) x) dx \times \int_{-\infty}^{\infty} T(k) \frac{\exp\{ik(\tilde{x} - \tilde{x}') + i\kappa_a(\tilde{z} - \tilde{z}')\}}{\kappa_a} dk, \quad (4)$$

The above two integrals can be evaluated analytically, and the final result is

$$S(\theta, \alpha) = \frac{-1}{16\pi^3} \gamma(\omega) \omega \rho_f A_{\mathcal{T}} A_{\mathcal{R}} \frac{T(k_a \sin(\theta))}{k_a \cos \theta} \times \exp\{-ik_a \sin \theta \tilde{x}' + ik_a \cos \theta(\tilde{z} - \tilde{z}') + k_a b \sin \theta \sin \alpha\}. \quad (5)$$

It can be shown that the expression in Eq (5) is in fact a transmission coefficient weighted by the spatial Gaussian beam spectrum; To recover the entire transmission spectrum, we must sum the spectra obtained at many incident angles, depending on the spectral width of the incident beam, according to  $T_s(\theta) = \sum_{\alpha} S(\theta, \alpha)$ , where  $T_s$  is the sum of spectra at multiple values of  $\alpha$ , and when  $T_s$  is normalized by the window function of the corresponding incident beams, it will be identical to the plane-wave transmission coefficient, as we show later.

For a 3-D voltage calculation we have, using spherical coordinates,  $k_x = k_a \sin \theta_i \cos \phi_i$ ,  $k_y = k_a \sin \theta_i \sin \phi_i$ , and  $k_z = \kappa_a = k_a \cos \theta_i$ . The transformed signal is

$$S(\alpha, \theta) = \frac{-1}{8\pi^2} \gamma(\omega) \omega \rho_f A_{\mathcal{T}} A_{\mathcal{R}} \frac{1}{2\pi} \int_{-\infty}^{\infty} \exp(-ik_a x \sin(\theta)) dx \int_0^{2\pi} \int_0^{\pi/2-i\infty} T(\theta_i, \phi_i) \times \exp \{ ik_a (\sin \theta_i \cos \phi_i (\tilde{x} - \tilde{x}') + \cos \theta_i (\tilde{z} - \tilde{z}')) \} k_a \sin \theta_i d\theta_i d\phi_i. \quad (6)$$

The integration over  $x$  produces a Dirac  $\delta$  function,

$$S(\alpha, \theta) = \frac{-1}{8\pi^2} \gamma(\omega) \omega \rho_f A_{\mathcal{T}} A_{\mathcal{R}} \int_0^{2\pi} \int_0^{\pi/2-i\infty} T(\theta_i, \phi_i) \times \exp \{ -ik_a (\sin \theta_i \cos \phi_i \tilde{x}' + \sin \theta_i \cos \phi_i b \sin \alpha + \cos \theta_i (\tilde{z} - \tilde{z}')) \} \times \delta(k_a \sin \theta_i \cos \phi_i - k_a \sin \theta) k_a \sin \theta_i d\theta_i d\phi_i, \quad (7)$$

where further simplifications are possible.

## EXPERIMENTAL TECHNIQUE

Our AC ultrasound experiment is conducted with two capacitance foil transducers, one used as transmitter, and the other as receiver. They have an effective radius of 5 mm and a center frequency of 0.7 MHz with a usable response from 0.1 MHz to about 1.5 MHz. A Parker-Daedel positioning system with a repeatability of 0.02 mm is used for the position scans performed here. The transducers are mounted on precision rotary stages with a usable angular resolution of 0.01°. The transmitter is excited by a high voltage tone burst of 10 to 20 cycles with frequency from 0.2 MHz to 1.5 MHz. The transmitted signal is detected by an identical capacitive foil receiver and fed to a Cooknell CA6/C charge preamplifier and bias circuit. The receiver signal is further amplified by a broadband RITEC amplifier, and the rf signal is sent to a Lecroy 9304 oscilloscope to be digitized. At each scan step, the digitized waveform is sent to a DEC workstation, where we first perform a FFT on the time-domain signal and extract the frequency component of interest. A spatial Fourier transform is constructed from the scan data to obtain the angular spectrum. The sum of the angular spectrum of different incident angles is the reconstructed transmission coefficient.

## RESULTS AND DISCUSSION

Before presenting experimental results, we perform a theoretical calculation to illustrate the reconstruction strategy. Shown in Fig. 2 is the transmitted signal of a Plexiglas plate of 2.57mm as a function of scan coordinate calculated from Eq (3). For the solid curve, the incident angle of 15° lies between two Lamb mode phase matching angles, so both modes are excited, as can be confirmed by observing the

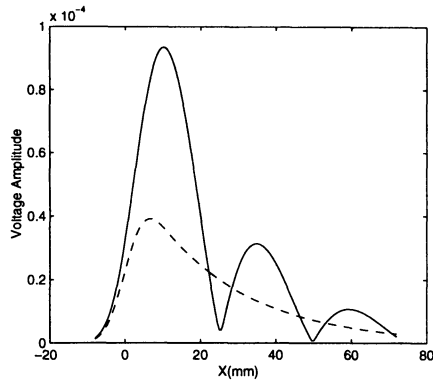


Figure 2. Transmitted signal calculated from Eq. (3) (with the plane-wave transmission coefficient) for a Plexiglas plate at an incident angle of  $15^\circ$  (solid curve) and  $8.5^\circ$  (dashed curve) as a function of scan coordinate  $x$ .

interference beyond  $x = 20$  mm. For an incident angle of  $8.5^\circ$ , only one mode is excited, and a monotonic decrease beyond  $x = 20$  mm is observed.

The angular spectra calculated from synthetic data for the scans detailed above are shown in Fig. 3(a). The solid curve is the Fourier transform of the theoretical finite scan shown in Fig. 2, while the dashed line is the result calculated from Eq (5), which assumes an infinite scan. A careful examination of the plots shows that the solid curve has some very small oscillations in the tails of the distribution. The dip between the two modes is also slightly deeper. These differences arise from the finite nature of the scan. In fact the solid curve is a convolution of the dash curve with a sinc function, which is the Fourier transform of a rectangular window. Figure 3(b) illustrates the physical significance of Eq (5). The angular spectrum of incident beam around the incident angles is superimposed on the plane-wave transmission coefficient, and the two scans with incident angles of  $8.5^\circ$  and  $15.5^\circ$  recover only the portion of the transmission coefficient which is subtended by the incident beam angular spectrum.

We now sum the spectra at several incident angles to recover a function related to the transmission coefficient. Such a summation is shown in Fig. 4. The sum of 20 spectra at different incident angles from  $1^\circ$  to  $20^\circ$  calculated from Eq (5) is shown in Fig. 4(b) as dash-dotted curve, while the solid curve is the plane-wave transmission coefficient. Both are normalized by their maximum value. A small difference appears at lower phase matching angles and can be explained as the effect of the finite aperture window shown in Fig. 4(c). The slope of the window at the lower phase matching angle reduces slightly the amplitude of the transmitted signal. In order to reconstruct the plane-wave transmission coefficient completely, the transmitted signal must be normalized by the corresponding aperture window under the same experimental conditions. This conclusion is confirmed by the results shown in Fig. 4(a). The solid curve is the transmission coefficient. The dashed line is the transmitted signal normalized by the window in Fig. 4(c), and it corresponds exactly to the plane-wave transmission coefficient.

Although the sum of 2-D calculated voltage spectra for an infinite, window-normalized coordinate scan is approaches the plane-wave transmission coefficient, the 3-D voltage calculation shows this equality no longer holds, even for an

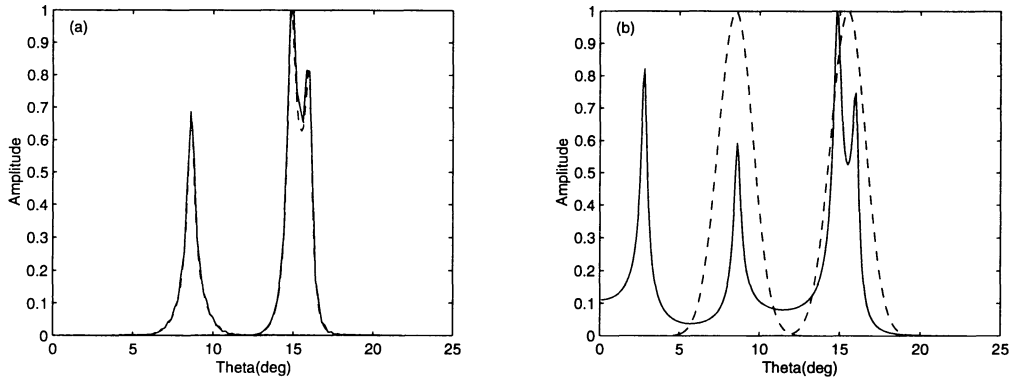


Figure 3. (a) Comparison of angular (spatial) spectra (solid curve) of the  $x$ -scan data at incident angles of  $8.5^\circ$  (first sharp peak) and  $15.5^\circ$  (second two peaks) in the previous figure and a direct calculation (dashed curve) using Eq. (4); (b) a physical illustration of Eq. (4).

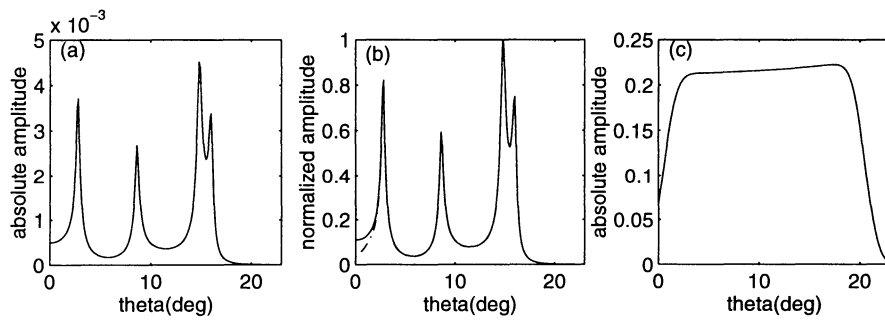


Figure 4. (a) Plane-wave transmission coefficient (solid curve) and 2-D synthetic reconstructed signal normalized by window (dashed curve); (b) Transmission coefficient (solid line) and the 2-D synthesized transmitted signal not normalized by window at right; (c) Window produced by summing the angular spectra of several incident angles with no plate.

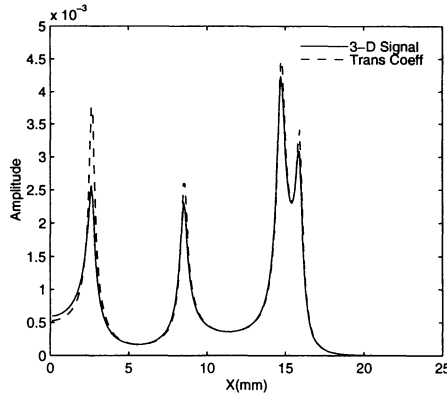


Figure 5. Comparison of plane-wave transmission coefficient (dashed curve) and reconstructed transmission coefficient from 3-D voltage calculation when the object distance is 30 mm.

infinite scan. Shown in Fig. 5 is a comparison between a 3-D normalized spectral sum and the plane-wave transmission coefficient. The difference is obvious, especially at low phase matching angles. The origin of the disparity can be explained by an examination of the wavevector geometry. According to Eq (7) it is the wavevector satisfying  $k_a \sin \theta_i \cos \phi_i = k_a \sin \theta$  or  $\sin \theta_i = \sin \theta / \cos \phi_i$  that makes a contribution to the voltage; when  $\theta$  is smaller, the range of  $\phi_i$  will be larger, and the effects of  $\phi_i$  will also be more significant.

The difference in the voltage arises from a comparison between a 2-D Gaussian beam and a rotationally symmetric Gaussian beam. For a Gaussian sheet beam all rays lie in the incident plane. The spatial Fourier transform extracts a wavevector spectrum from the  $x$ -scan data. At any particular incident angle, only the rays in the incident beam whose projection along the  $x$ -axis match a certain wavevector make a contribution to that wavevector in the final reconstructed transmission coefficient. The projection of those out-of-plane rays onto the  $x$ -axis for a rotationally symmetric Gaussian beam is different from the inplane ray and this difference depends on the phase match angle. Differences between the plane-wave transmission coefficient and the reconstructed transmission function arise from two principal causes: one is the finite  $x$ -scan, and the other is diffraction of real 3-D beams. The finite scan has an effect similar to the finite window function in digital signal processing. The error resulting from the finite scan is actually very small in most cases and is not our main focus. In the following experiments and their inversion we will pay particular attention to the effects of beam diffraction on the transmission function.

The low acoustic impedance of Plexiglas makes it ideal for air-coupled experiments, and the low noise floor in the experimental data is shown in Fig. 6 (solid curve). In frame (a) the experimental data are fitted with the reconstructed 3-D voltage transmission function which is represented as a dashed curve. The best fit gives  $c_l = (2.74, -0.03)$  and  $c_t = (1.38, -0.018)$  for the real and imaginary parts of the two velocities in km/sec. The same data set can also be fitted with plane wave transmission using the same algorithm, which gives  $c_l = (2.74, -0.063)$  and  $c_t = (1.38, -0.018)$  in km/sec, and is also represented by a dashed curve in frame (b). We see that the only difference is in the imaginary part of  $c_l$ . The reconstructed

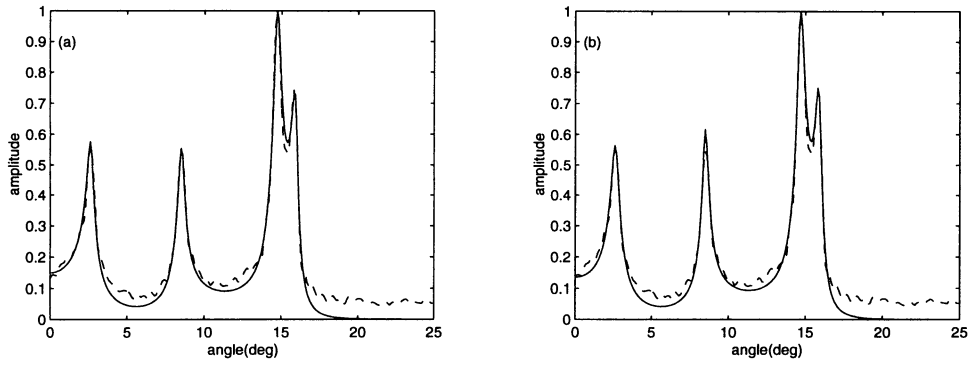


Figure 6. (a) Inversion of experimental data by reconstructed transmission coefficient  $T_r$ ; (b) inversion of experimental data by the plane-wave transmission coefficient. Two approaches give different constants. See text.

transmission functions have the same peak positions as the plane-wave transmission coefficient, since these are determined by the real parts of  $c_l$  and  $c_t$ . We've already seen that beam diffraction can have a strong effect on the amplitude of the reconstructed transmission function at low phase matching angle. The amplitude of the transmitted signal at low phase matching angle is crucial for determining the imaginary part of  $c_l$ .

The above method has been extended to anisotropic materials. We perform experiments both on a uniaxial graphite epoxy and biaxial graphite epoxy. Owing to space limitations, only the biaxial graphite-epoxy results are shown here. Our plates have a stacking sequence of  $[0, 90]_{3s}$ . Since the number of plies in the two fiber directions is the equal, according to lamination theory [7], the following relations among the elastic properties obtain,  $C_{11} = C_{22}$ ,  $C_{13} = C_{23}$ , and  $C_{44} = C_{55}$ . The assumption of lamination theory is justified by the relatively low frequencies employed in these air-coupled measurements. Thus, we have six independent stiffness constants,  $C_{11}$ ,  $C_{12}$ ,  $C_{13}$ ,  $C_{33}$ ,  $C_{44}$ ,  $C_{66}$ . Earlier we found at 1.1 MHz that the transmission coefficient is sensitive to  $\Re\{C_{11}\}$ ,  $\Re\{C_{13}\}$ ,  $C_{33}$ , and  $C_{44}$ , and also slightly dependent on  $\Im\{C_{11}\}$ ,  $\Im\{C_{13}\}$ . The transmission coefficient is almost independent of  $C_{12}$  and  $C_{66}$ . At 0.41 MHz, however, the transmission coefficient is almost completely dependent on  $\Re\{C_{11}\}$  and  $C_{44}$ . So our approach is first to determine  $C_{11}$  and  $C_{44}$  by using the data at 0.41 MHz, and then to determine  $C_{13}$  and  $C_{33}$  by using data of 1.1 MHz. An experimental transmission function measured at 0.41 MHz is shown in Fig. 7(a) as a solid curve, where only the  $A_0$  mode can be seen. A theoretical analysis indicates that the Lamb mode near  $3^\circ$  is determined by  $C_{11}$ . This mode is found in water immersion testing and can be used to determine  $C_{11}$ , which we have found is 71.3 GPa. Knowing  $C_{11}$ , an inversion that determines two constants  $\Re\{C_{44}\}$  and  $\Im\{C_{44}\}$  can be easily performed, and the result is  $C_{44} = 5.24 - 0.43i$ . The corresponding fitted curve is shown as a dashed trace in Fig. 7(a). With the knowledge of  $C_{11}$  and  $C_{44}$ , we can proceed to invert  $C_{13}$  and  $C_{33}$  from the experimental data of 1.1 MHz. The results are shown in Fig. 7(b), where the best fit gives  $C_{13} = 3.45 - 0.085i$  and  $C_{33} = 15.83 - 0.49i$ .

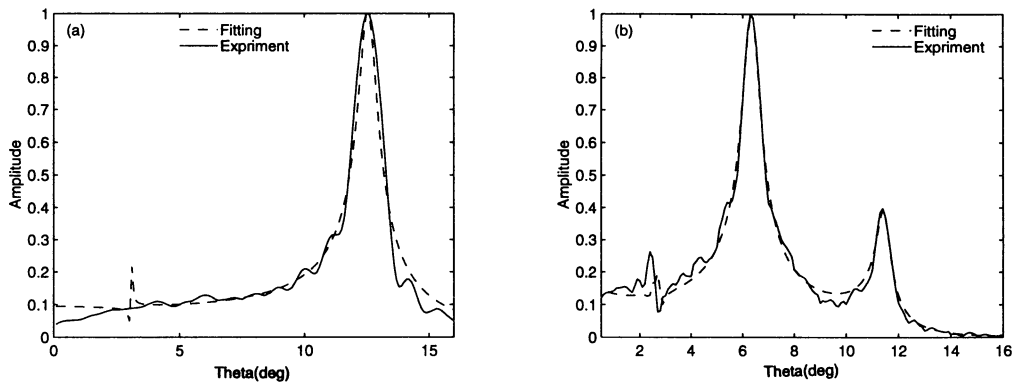


Figure 7. The reconstructed transmission coefficient (solid curve) of a biaxial graphite epoxy laminate and best fit results (dashed curve). (a)  $f=0.41\text{MHz}$ , (b)  $f=1.1\text{MHz}$ .

## CONCLUSION

In this paper we have reformulated the problem of voltage calculations in two- and three-dimensional beam geometries in terms of the mathematically efficient complex transducer point. We have analyzed, in particular, the influence on the reconstructed transmission function of rays lying outside the incident plane. We find that the difference between the reconstructed transmission functions obtained by using the transducer voltage calculated from a Gaussian sheet beam and a rotationally symmetric 3-D Gaussian beam are not large, but may, under some conditions, be significant. The difference is especially large near normal incidence. The sheet beam reconstructs identically to the plane-wave transmission coefficient, while the 3-D beam gives a result that differs solely in the relative amplitudes of the transmission peaks and valleys.

## REFERENCES

1. D. E. Chimenti, *Appl. Mech. Rev.*, **50**, 247–284 (1997).
2. S. I. Rokhlin and D. E. Chimenti, *Review of Progress in Quantitative NDE*, **9**, Eds. D. O. Thompson and D. E. Chimenti, (Plenum, New York, 1990), 1411–1418.
3. D. W. Schindel, D. A. Hutchins, L. Zhou and M. Sayer, *IEEE Trans. Ultrason. Ferroelect. Freq. Contr.* **42**, 42–50 (1995).
4. A. Safaeinili, D. E. Chimenti, and O. Lobkis, *IEEE Trans. Ultrason. Ferroelect. Freq. Contr.* **43**, 1171–1180 (1996).
5. S. Zeroug, F. E. Stanke, and R. Burrige, *Wave Motion*, **24** 21–40 (1996).
6. O. I. Lobkis, D. E. Chimenti, Han Zhang, M. Rudolph, *Review of Progress in Quantitative NDE*, **17**, *op. cit.*, 1139–1146, (Plenum, New York, 1998).
7. T. H. Hahn, W. Stephen, *Introduction to composite materials*, Lancaster, PA (1980).